Intermittent pili-mediated forces fluidize Neisseria meningitidis aggregates promoting vascular colonization

Daria Bonazzi, Valentina Lo Schiavo, Silke Machata, Ilyas Djafer-Cherif, Pierre Nivoit, Valeria Manriquez, Hirokazu Tanimoto, Julien Husson, Nelly Henry, Hugues H Chaté, et al.

▶ **To cite this version:**

Daria Bonazzi, Valentina Lo Schiavo, Silke Machata, Ilyas Djafer-Cherif, Pierre Nivoit, et al.. Intermittent pili-mediated forces fluidize Neisseria meningitidis aggregates promoting vascular colonization. Cell, 2018, 174 (1), pp.143 - 155.e16. 10.1016/j.cell.2018.04.010 . hal-01871317

HAL Id: hal-01871317
https://hal.science/hal-01871317

Submitted on 21 Sep 2018

HAL is a multi-disciplinary open access archive for the deposit and dissemination of scientific research documents, whether they are published or not. The documents may come from teaching and research institutions in France or abroad, or from public or private research centers.

L'archive ouverte pluridisciplinaire **HAL**, est destinée au dépôt et à la diffusion de documents scientifiques de niveau recherche, publiés ou non, émanant des établissements d'enseignement et de recherche français ou étrangers, des laboratoires publics ou privés.

Intermittent pili-mediated forces fluidize *Neisseria meningitidis* aggregates promoting vascular colonization

D. Bonazzi[1†], V. Lo Schiavo[1†], S. Machata[1], I. Djafer-Cherif[2], P. Nivoit[1], V. Manriquez[1], H. Tanimoto[3], J. Husson[4], N. Henry[5], H. Chaté[2,6,7], R. Voituriez[5,7], G. Duménil[1*]

Affiliations :

[1] Pathogenesis of Vascular Infections, Institut Pasteur, INSERM, Paris, France.

[2] Service de Physique de l'Etat Condensé, CEA, CNRS, Université Paris-Saclay, France.

[3] Institut Jacques Monod, Paris, France.

[4] Laboratoire d'Hydrodynamique (LadHyX), Department of Mechanics, Ecole polytechnique-CNRS UMR7646, 91128 Palaiseau, France.

[5] Laboratoire Jean Perrin, CNRS/UPMC, Paris, France.

[6] Computational Science Research Center, Beijing 100193, China.

[7] LPTMC, Université Pierre et Marie Curie (CNRS/UPMC), Paris, France.

*Correspondence to: guillaume.dumenil@pasteur.fr

† *Authors contributed equally to this work.*

Abstract

Neisseria meningitidis, a bacterium responsible for meningitis and septicemia, proliferates and eventually fills the lumen of blood capillaries with multicellular aggregates. The impact of such an aggregation process and its specific properties are unknown. We first show that aggregative properties are necessary for efficient infection and study their underlying physical mechanisms. Micropipette aspiration and single cell tracking unraveled unique features of an atypical fluidized phase, with single cell diffusion exceeding that of isolated cells. Quantitative description of bacterial pair interactions combined with active matter physics based modeling showed that this behavior relies on type IV pili active dynamics, which mediate alternating phases of bacteria fast mutual approach, contact and release. These peculiar fluid properties are found to be necessary to adjust to the geometry of micro-channels mimicking capillaries upon bacterial proliferation. Intermittent attractive forces thus generate a fluidized phase that allows efficient colonization of the blood capillary network during infection.

Introduction

Mechanisms and principles driving bacterial aggregation are highly diverse as they depend on the specific properties of the bacterial species involved and the conditions they live in. Bacterial aggregates in the context of biofilms for instance are the focus of intense study because of their clinical importance as a mechanism of antibiotic resistance. Their mechanical properties are largely defined by the self-produced matrix composed of DNA, polysaccharides and proteins, which behave as a hydrated polymeric meshwork. Such structures display viscoelastic properties combining both viscous fluid and elastic behavior (Persat et al., 2015). A second type of bacterial aggregates relies on bacterial motility. In particular, *Escherichia coli* or *Salmonella typhimurium* are able to form clusters of different shapes and sizes which depend on flagella-based motility and chemotactic cues (Budrene and Berg, 1991).

Another example of motility-driven aggregation is that of *Neisseria gonorrheae*. In this case, the retractile properties of their long filamentous organelles known as type IV pili (T4P), allow them to move on surfaces, a process known as twitching motility. Combined with interactions between pili this motility promotes bacterial clustering (Oldewurtel et al., 2015; Taktikos et al., 2015). In addition to *Neisseria gonorrhoeae*, T4P are expressed by a large number of Gram-negative bacteria including human pathogens such as *Vibrio cholera*, *Pseudomonas aeruginosa* or *Neisseria meningitidis* as well as Gram-positive bacteria such as *Streptococcus sanguinis*. T4P are several microns long semi-flexible fibers extending out of the bacterial body. In *Neisseria spp.* pili are highly dynamic as they grow and retract at speeds in the order of 1 µm/s. As they retract through an ATP-dependent process, individual pili can generate very high forces, reaching up to 100 pN for single pili and ten-fold this value for bundles of pili (Biais et al., 2008; Maier et al., 2002). Pilus-pilus interaction is thought to promote auto-aggregation.

In *Neisseria meningitidis*, T4P are central virulence factors required for bacterial adhesion along the endothelium and subsequent formation of intravascular aggregates. This vascular colonization process is a prerequisite for vascular damage observed during infection

(Melican et al., 2013). *In vitro* studies have shown that aggregates formed by *N. meningitidis* also depend on type IV pili but the biophysical properties of these clusters and their impact on the infection process have not been characterized. Once bacteria adhere to capillary endothelial cells, they proliferate and progressively occlude the vessel lumen. Growth in the tubular and sometimes tortuous geometry found in capillaries imposes important mechanical constraints that require specific adaptation. This interdisciplinary work explores how the biophysical properties of *N. meningitidis* aggregates determines human disease progression.

Results

Auto-aggregation enhances vascular colonization *in vivo*

During meningococcal infection, bacterial aggregates can be found in the lumen of capillaries located in most organs including the brain, but the impact of aggregation on disease progression is unknown (Mairey et al., 2006). Such aggregates also form in human capillaries of a humanized mouse model based on human skin xenograft, which reproduces the key histological features of *N. meningitidis* infection (Melican et al., 2013). In such a model, we observed that aggregates filled the vessel lumen 6h post-infection while adjusting to the complex, sometimes anastomosed capillary network over tens to hundreds of µm (Figure 1A). To assess the role of aggregation, we exploited a naturally occurring variant of the major pilin termed $PilE_{SA}$ (Nassif et al., 1993). This variant occurred spontaneously through a genetic recombination system present in *Neisseria* species (Rotman and Seifert, 2014). In contrast with the frequently occurring $PilE_{SB}$ variant that promotes both adhesion and aggregation, the $PilE_{SA}$ variant selectively promotes adhesion but not aggregation (Figure S1A). Individual bacteria from a strain expressing the SA and SB pilin variants had the same ability to adhere to endothelial cells in the presence of flow and proliferated at the same rate (Figures S1B and S1C). However, *in vitro,* single adhering bacteria of the $PilE_{SB}$ variant formed 3D densely packed microcolonies on the cellular surface upon proliferation, while the $PilE_{SA}$ variant led to more dispersed, 2D microcolonies formed by a single bacterial monolayer (Figures S1D and S1E). *In vivo*, the aggregative capacity of bacteria did not affect survival in the blood of infected animals (Figure 1B). At the initial time points of infection (6h) aggregation had little effect on the ability of the bacteria to accumulate along vessels, but after 24h the non-aggregative strain showed a 60-fold decrease in bacteria number in the human skin compared to the aggregative one (Figure 1C). These results show that bacterial auto-aggregation is important for disease progression, and underline the ability of aggregates to highly deform in order to adapt to the complex geometry of the microcirculation.

Neisseria meningitidis aggregates display a viscous liquid behavior in suspension

The above results raised the question of the physical mechanisms governing the formation and dynamics of *N. meningitidis* aggregates. Interestingly, several properties of aggregates formed *in vitro* were reminiscent of the behavior of liquid droplets. In liquid suspension, *N. meningitidis* cells spontaneously formed quasi-spherical, dynamic aggregates that tended to sediment to the bottom of the wells without adhering to the surface (Figures 2A and S2; Movie S1). In addition, when two aggregates came in close proximity, they rapidly fused and relaxed to a larger, spherical aggregate within a few minutes (Figures 2B, S3A, S3B, S3C and S3D; Movie S1), suggesting that they can be described as a liquid phase endowed with an effective surface tension. This viscous liquid behavior was also corroborated by wetting experiments in which progressive aggregate spreading on an adhesive surface could be observed by TIRF microscopy (Figures S3E, S3F and S3G). To quantify the mechanical properties of this phase, we adapted a micropipette aspiration protocol to our system (Guevorkian et al., 2010; Guevorkian et al., 2011): the application of a constant negative pressure on a bacterial aggregate led to its deformation inside the micropipette (Figures 2C and 2D, movie S2). Interestingly, in the range of applied pressures (10-100 Pa), the length of the tongue increased linearly over time, indicating a purely viscous liquid behavior (Figure 2E). By analyzing the dynamics of the aggregates and further applying the Laplace law, we could obtain estimations of the aggregate viscosity (9 Pa.s) and surface tension at rest (0.1 mN/m; Figures 2F and 2G). Thus, aggregates of *N. meningitidis* exhibit a liquid-like behavior with no elastic component even at short time scales. As a comparison, values of viscosity and surface tension for common viscous liquids can be found in Supplementary Table 1. The viscosity of *N. meningitidis* aggregates is close to that of honey (2-10 Pa.s), with however a surface tension that is much lower than the one of honey (50-60 mN/m).

Diffusion of bacteria inside the aggregates reaches values higher than individual bacteria in suspension

To gain insights into the interactions driving this viscous behavior we then moved to a smaller scale and characterized the motion of single fluorescently-labeled wild-type (WT) bacteria inside aggregates, 30-40 μm in diameter, using spinning disk confocal imaging at high spatio-temporal resolution (Figures 3A, S4A and S4B; Movie S3). We characterized the movement of individual bacteria by an effective 2D diffusion coefficient. These results showed that this coefficient was small for bacteria close to the aggregate center of mass (COM), and progressively increased with the distance from the center (d_{COM}) reaching maximal values at the aggregate periphery. The relationship between bacterial diffusion coefficient and distance to the center was confirmed over multiple aggregates (n=20) after normalization for aggregate size (Figure 3B). The values of diffusion coefficients corresponding to a ~10 μm thick outer layer (0.3 - 0.5 $\mu m^2/s$) exceeded the diffusion coefficient of single freely diffusing bacteria (Figures 3B and 3C). Diffusion of individual diplococci in suspension in liquid medium was determined experimentally to be 0.25 $\mu m^2/s$ and was not affected by piliation as a non-piliated strain (*pilD*) exhibited the same motility, consistently with the passive diffusive motion of a 1 *μ*m diameter particle in water. This feature stands in contrast to ordinary liquids at equilibrium, where attractive intermolecular forces ensure cohesion and slow down particle motion compared to the gas phase. In the case of *N. meningitidis* bacterial aggregates, we found on the contrary that individual bacteria within the aggregate (liquid phase) exhibit an apparent diffusion coefficient higher than non-interacting single bacteria outside of the aggregate (dispersed or gas-like phase). Pursuing the analogy with the movement of particles of a classical fluid in a liquid or dispersed phase, we concluded that this active system displays an anomalously fluidized phase, the origin of which deserves further clarification.

Pairwise interaction between bacteria shows cycles of attraction and release

In order to elucidate the origin of the unusual properties of *N. meningitidis* aggregates, we focused on the likely elementary building block of bacterial aggregation, *i.e.* the interactions between two cells. To this aim, we performed time-lapse microscopy of 2-10 isolated WT

bacteria confined in quasi-2D circular microfabricated (width = 50 µm, height = 10 µm) agar chambers (Figure 4A). Bacteria were prevented to interact with the glass substrate by passivation with a hydrophobic molecule (PLL-PEG) and no evidence of twitching motility could be observed in these conditions (Figures S4C and S4D). Bacteria diffused freely in the chambers, until two of them rapidly moved towards each other and got in close contact (Figure 4B and Movie S4). After a variable contact time, bacteria detached and eventually resumed free diffusion or undertook a new phase of attraction, possibly with another cell. Detection of these “active pulling” events was implemented in a semi-automatic script based on the analysis of interbacterial distance and its first derivative as a function of time (Figure 4C). The active pulling events were T4P-dependent, since non-piliated bacterial mutants (e.g. *pilD*) failed to display them. Analysis of over 100 events of interacting bacteria provided a quantitative description of the elementary process initiating aggregation (Figures 4D, 4E, 4F and 4G). For instance, mean interbacterial distance at the beginning of a pulling event was 6.9 µm but could reach up to 20 µm (Figure 4D). This is in agreement with previously reported measurements of average T4P length of the same strain by immunofluorescence (Imhaus and Dumenil, 2014). Furthermore, a mean approaching speed of 1.5 µm/s (Figure 4E) during attraction sequences is in line with previous measurements using optical tweezers (Merz et al., 2000). Another signature of the attractive phase was given by the average interaction angle, defined as the angle between each single bacterial step and the axis intersecting the two bacteria, which was narrowly centered around 0 during interaction events underlining the high directionality of the mutual approach (Figure 4E, inset). Most importantly, and for the first time, this approach allowed to quantify the time intervals bacteria spent attracting each other (ON phase) or not (OFF phase) once they fall within the interaction range (20 µm). Probability distribution function of the ON and OFF phase durations followed an exponential decay with strikingly similar characteristic times, namely t_{ON} = 15.5 s and t_{OFF} = 16.3 s (Figures 4F and 4G). Analysis at the level of individual pairs of cells thus demonstrated an intermittent interaction process and provided the key parameters characterizing the T4P-mediated pairwise interaction between bacteria.

An intermittent attractive force between particle pairs is sufficient to recapitulate aggregate properties

The above results prompted us to investigate the role of intermittent attractive forces between bacteria as the physical basis of the highly fluidized phase formed by *N. meningitidis* aggregates. We hence built a 2D minimal model of active fluid in order to assess how an intermittent active process of rapid attraction between bacteria could relate to the overall unique material properties of aggregates (Supplementary Information model). Models have been previously used to describe the interaction of single *N. gonorrheae* cells with an abiotic surface (Marathe et al., 2014; Weber et al., 2015). Here, in order to analyze aggregation properties, we rather built and parametrized the model for numerical simulations focusing on the pairwise *N. meningitidis* bacterial interactions, characterized quantitatively in the micro-chambers (d_{int}, v_{int}, D, t_{ON} and t_{OFF}). Bacteria were modeled as apolar circular solid particles interacting via a pairwise potential with a hard-core repulsion reflecting the cell finite size. The T4P-dependent attachment and active pulling were modelled via an attractive force, which was stochastically turned ON and OFF for pairs of particles that were (i) within a cut-off distance (defined as twice the maximal pili length) and (ii) neighbors as defined by a Voronoi tessellation plane partitioning (Figure 5A). In effect, this restriction to Voronoi neighbors favored interactions within a first circle of an average of 6 neighbors, which corresponds to the experimentally determined average pili number per bacterium (Imhaus and Dumenil, 2014). With these simple assumptions and experimentally determined parameters, simulated particles in a pair could undergo a cycle during which they attached, moved towards each other, remained in contact and finally detached (Figure 5B). At higher particle densities, initially randomly dispersed particles progressively organize in dynamic round-shaped aggregates that occasionally fused and formed a new larger and circular cluster (Figure 5C). *In silico* simulated large groups of particles displayed apparent diffusion coefficients in complete agreement with the experimental results of bacterial motion inside aggregates, remarkably requiring no parameter adjustment (Figure 5D). Moreover, the

spatial distribution of diffusion coefficients was conserved, with low diffusion at the aggregate center and increasing values going outward, reaching values higher than free diffusion at the aggregate periphery (Figure 3K, dotted line). Aggregates of particles intermittently attracting each other thus exhibit a liquid-like behavior with high diffusion confirming that the active intermittent interaction is sufficient to reproduce the highly diffusive fluidized phase of real aggregates. A mean field analysis (SI Model) confirmed that the observed high diffusion properties can be attributed to the intermittent dynamics of the pili, which act as an active source of noise in the system. Intermittent attractive forces thus promote efficient aggregate formation combined with a fluidization effect due to high particle diffusion.

Intermittent attractive properties between bacteria define a phase diagram of aggregation phenotypes

To test the reach of the model we examined its main prediction: aggregate material properties are controlled by the ratio of the time spent in the OFF (no attraction) and the ON (attraction) phases (i.e. t_{OFF}/t_{ON}). Accordingly, aggregate simulations at constant t_{ON} = 15 s while modulating t_{OFF} led to different states of matter (Figure 6A and movie S5): a dispersed gas-like phase where no aggregates formed at high values of t_{OFF}/t_{ON}, a liquid phase with dynamic aggregates with t_{OFF}/t_{ON}*~1*, and finally a solid phase with frozen crystal-like aggregates for low values of t_{OFF}/t_{ON}. To quantitatively determine these phase transitions, we used the average particle diffusion coefficient in the aggregate to determine solid-to-liquid transition, and the dynamic stability of large aggregates defined by the radius of gyration for the liquid-to-gas transition (Figure 6B). Interestingly, these simulations indicate that the average diffusion coefficient curve peaked at a t_{OFF}/t_{ON} ratio equal to 1, very close to the value measured experimentally with WT bacteria. Importantly, particles in the external layer of the simulated aggregates showed a higher effective diffusion constant compared to individual particles (0.25 $\mu m^2/s$) thus recapitulating the high diffusion regime observed at the periphery of WT bacterial aggregates (Figure 6B, dashed line). Properties of T4P interaction

corresponding to a t_{OFF}/t_{ON} ratio equal to 1 which were observed with WT bacteria thus correspond to a maximum of intra-aggregate bacterial diffusion. Finally, we built up a complete phase diagram in the t_{ON} - t_{OFF} space by independently varying both parameters (Figure 6C). Numerical simulations were in agreement with mean-field analysis and showed that the actual balance between the time spent in the ON and OFF phases, the t_{OFF}/t_{ON} ratio, dictates the aggregative properties of the system (SI model).

To complete the model validation, we tested its predictions by genetically manipulating bacteria. Slightly decreasing the t_{OFF}/t_{ON} ratio was predicted to strongly reduce intra-aggregate diffusion and thus increase viscosity (Figure 6D). *N. meningitidis* expresses a thick capsule at its surface composed of polymers of negatively charged sialic acid residues in the serogroup C strain used here. Mutants devoid of capsule (*siaD*) were still able to form aggregates but became “stickier” than their wild-type counterparts, thus displaying larger contact times and a corresponding decrease in the t_{OFF}/t_{ON} ratio (Figures 6C and 6E; Movie S6). The results corroborated the model predictions showing that a low t_{OFF}/t_{ON} ratio decreased the intra-aggregate bacterial diffusion and flattened the spatial distribution of the diffusion values (Figure 6F). Accordingly, micropipette measurements showed that non-capsulated mutants form more viscous aggregates (50 Pa.s, Figure 6G). Symmetrically, a slight increase in the t_{OFF}/t_{ON} ratio was predicted to fluidize the aggregate core and hence to decrease the overall viscosity (Figure 6H). In particular, the spatial distribution of diffusion coefficients was predicted to progressively flatten by increasing t_{OFF}/t_{ON}, with simulated particles in the aggregate center being more motile while particles at the boundaries being less motile compared to the simulation of the WT case (Figure 6H). To increase t_{OFF}/t_{ON} in our biological system, we reduced the number of pili expressed by bacteria (Imhaus and Dumenil, 2014) and hence decreased the probability of attraction. As predicted by the model, bacteria at 60% piliation level compared to WT exhibited a flattened distribution of effective diffusion coefficients within the aggregate (Figure 6J). Micropipette aspiration showed a linear relationship between the average number of pili per cell and the viscosity of the aggregate (Figure 6K). In conclusion, by experimentally varying the probabilities of

attraction and separation between real bacteria using genetics we could modulate the physical properties of the bacterial aggregates as predicted by the model. Remarkably, the specific properties of bacterial interactions in the unmodified WT *N. meningitidis* place it in the phase diagram in a narrow region prone to the formation of viscous liquid aggregates fluidized by high intra-aggregate diffusion.

Fluid-like behavior of aggregates favors colonization of capillary mimics

We then asked whether this intermittent attractive force generated fluidization effect of *N. meningitidis* aggregates could have a function in their capacity to invade capillaries. The viscous aggregates highlighted in our study are highly deformable and this could allow the adaptation to the particular geometry of the microcirculation during bacterial proliferation. To test this hypothesis, we used a bacterial mutant that forms aggregates but fails to display intermittent attractive forces. The *pilT* mutant, lacking the ATPase responsible for pilus retraction, is able to form contacts through its abundant pili but fails to detach (Figure 7A). As predicted, aggregates of the *pilT* mutant were not round shaped, did not flow into the pipette even at high aspiration pressures and individual bacteria failed to diffuse in the aggregates indicating a solid material totally devoid of fluid properties (Figures 7A, 7B and 7C; Movie S6). To test the ability of aggregates to adjust to the capillary geometry following volume increase due to bacterial proliferation, *pilT* and WT bacteria were allowed to grow in 10 µm-wide PDMS (polydimethylsiloxane) channels to mimic capillary dimensions. WT aggregates grew in a continuous fashion while rapidly adjusting to the imposed channel geometry (Figure 7D and Movie S8). Aggregate size increased over time due to cell proliferation and occasional aggregate fusion with neighboring colonies (Figure 7E). In contrast, the solid-like *pilT* colonies initially grew as WT until they filled up the whole channel section, increased bacterial density and then stopped growing. From these results, we conclude that the viscous properties of the aggregates can determine the evolution of the infection process by favoring space occupancy in the particular geometry of the capillary network.

Discussion

Analysis of human cases as well as studies conducted with a humanized animal model revealed that aggregates of *Neisseria meningitidis* were able to adapt to the shape of the infected vessels, reaching high aspect ratios and complex morphologies. Here we show that during infection bacterial aggregation is not only a side effect of proliferation but an active process due to specific physical properties of *N. meningitidis* bacteria-bacteria interactions.

Beyond the simple property of sticking together, the viscous-like properties of the aggregates are a determining feature of the infection process. As bacteria proliferate the environment of infected micro-vessels rapidly becomes a physical limit (Figure S5). The ability of *N. meningitidis* bacterial aggregates to quickly adapt to the vessel geometry through implementation of intermittent attractive forces could account for the exceptionally rapid disease progression of meningococcemia with rapid occupation of entire vascular networks and loss of organ function observed during *purpura fulminans*. Further studies will be necessary to evaluate whether other pathogens display similar properties and their impact on disease progression. In *Neisseria gonorrheae* for instance, a sorting phenomenon has been described upon changes in pilus posttranslational modifications highlighting a complex dynamics of aggregation in this species as well (Oldewurtel et al., 2015).

Our study further revealed a unique type of viscous material composed of particles endowed with higher diffusion coefficients in the liquid phase than in the dispersed gas phase. This is in contrast with the classical description of the gas phase which is defined by a higher diffusion of particles as compared to the liquid phase. This atypical high diffusion can be attributed to the intermittent dynamics of the interaction between particles, which acts as an additional source of noise in the system that fluidizes aggregates. In the context of infection, intermittent attractive forces between bacteria provide an optimum to combine efficient aggregation with a high diffusion required for low viscosity, leading to rapid adaptation to the geometry of blood capillaries during meningococcal infections. In addition to a better understanding of the physics behind the pathogenicity of *N. meningitidis*, our study uncovers novel design principles for materials with tunable viscosity.

Acknowledgements

Authors would like to thank Daiki Nishiguchi, Matthieu Piel and Ana-Maria Lennon-Dumenil for fruitful discussions and critical reading of the manuscript; Rafaele Attia and Jian Shi in Matthieu Piel's lab and Samy Gobaa from the Biomaterials and Microfluidics platform at the Institut Pasteur for technical advice and support in microfabrication. This work was supported by the ANR *agence national de la recherche* (GD); the *Fondation pour la Recherche Médicale* (GD and HC); the Integrative Biology of Emerging Infectious Diseases (IBEID) laboratory of excellence and by a European Research Council starting grant (GD). DB was funded by the Roux-Cantarini fellowship awarded by the Institut Pasteur.

Author contributions

This work represents the combined research directions of 2 groups (GD, RV/HC). *In vivo* experiments by SM and VM. Video-microscopy experiments of aggregate dynamics and microfabrication by DB. Micropipette aspiration experiments by VS, NH and JH. Image analysis by DB and HT. Modeling by IDC. All authors designed experiments. DB, GD, HC and RV wrote the paper.

Materials and Methods

Bacterial strains growth and mutagenesis

All *N. meningitidis* strains described in this study were derived from the recently sequenced 8013 serogroup C strain [http://www.genoscope.cns.fr/agc/nemesys] (Rusniok et al., 2009). Strains were streaked from -80°C freezer stocks onto GCB agar plates (Difco), and grown overnight in a moist atmosphere containing 5% CO_2 at 37°C. For all experiments, bacteria were transferred to liquid cultures in pre-warmed RPMI medium supplemented with 10 % FBS at adjusted OD600=0.05, and incubated with gentle agitation for 2 hours at 37°C in the presence of 5% CO_2. The *pilF pilF$_i$* strain was plated on GCB plates and then cultured in liquid media both containing IPTG in a range of 0 to 100 µM concentrations, depending on the level of piliation needed (Imhaus and Dumenil, 2014). Natural variants in the pilin gene, namely $PilE_{SA}$ and $PilE_{SB}$ strains, have been previously described (Nassif et al., 1993) and were fluorescently labeled by cloning the gene encoding GFP under the control of the pilE gene promoter. Mutations in *pilD* (Rusniok et al., 2009*)*, *siaD* (Brissac et al., 2012), *pilT* (Pujol et al., 1999) genes have been previously described. Bacteria were fluorescently labeled by cloning the gene encoding near infrared fluorescent protein iRFP (Filonov et al., 2011) under the control of the pilE gene promoter.

Cell culture

Primary HUVECs (PromoCell) were used between passages 1 and 10 and grown at 37°C in a humidified incubator under 5% CO_2 in Endo-SFM (Invitrogen) supplemented with 10% heat-inactivated FBS (Invitrogen) and 40 µg/ml of endothelial cell growth supplement (Harbor Bioproducts).

Xenograft model of infection

Introduction of human dermal microvessels into SCID/Beige mice by xenografting human skin was performed as previously described (Melican et al., 2013). For immunofluorescence, grafts were removed 6 hs post infection with GFP-expressing bacteria and fixed in 4%

paraformaldehyde (PFA). Samples were frozen in OCT (Tissuetek, Sartorius, USA) and sliced into 10mm fragments. Immunofluorescence was performed using Mouse on Mouse detection kit (Vector laboratories, Eurobio ABCys, France). Ulex Europaeus agglutinin Lectin-Rhodamine (Vector laboratories, Eurobio ABCys, France) was used to stain human vessels. Samples were mounted in Vectashield mounting reagent (Vector laboratories, Eurobio ABCys, France) and imaged on a spinning-disk confocal microscope.

Growth assay

Bacterial pre-cultures were diluted at initial OD_{600} = 0.05, loaded in a 96 well plate and incubated in a microplate reader (Cytation5, Biotek) under agitation at 37°C in the presence of 5% CO_2, with automated OD_{600} acquisition every 30 minutes for 18 hs.

Initial adhesion

Laminar flow experiments were performed as previously described (Mairey et al., 2006). Briefly, HUVECs were plated on 8-mm-diameter wells on glass slides coated with fibronectin (10 µg/ml) at a density of 10^4 cells/well. Cells grown on glass slides were placed in a parallel plate flow chamber and vacuum sealed. Experiments using the flow chamber were performed in Endo-SFM supplemented with 2% FBS at 37°C. Bacterial pre-cultures were diluted to OD_{600} = 0.075 and introduced into the chamber using a syringe pump (Vial Medical, Becton Dickinson, or Harvard Apparatus) at a shear stress of 0.044 dynes/cm^2. After 10 minutes of flow application, adherent bacteria were automatically detected and counted for multiple fields of view in the case of the pilin variants $PilE_{SA}$ and $PilE_{SB}$.

Bacteria proliferation on HUVECs

Time-lapse experiments were performed in Endo-SFM supplemented with 10% FBS at 37°C 5% CO_2. HUVECs were seeded into Ibidi µ-slides with Ibidi-treated plastic bottom (Ibidi) at a density of 10^4 cells/channel. Bacterial pre-cultures were diluted to OD_{600} = 0.02 (MOI = 200), loaded into the channels for 15 minutes at 37°C 5% CO_2 to allow bacterial adhesion and

finally washed 3X with fresh medium. Time-lapse movies of GFP expressing $PilE_{SA}$ and $PilE_{SB}$ bacterial strains proliferating on HUVECs were acquired over 4hs with a 20x phase objective. High resolution z-stacks of bacterial colonies were performed with a 100X objective (Z-step = 0.2µm).

Fusion of bacterial aggregates

Bacterial aggregates from a 2h pre-culture in RPMI + 10% FBS were loaded in a µ-dish chamber (Ibidi). Mineral oil was added on top to avoid evaporation. A micropipette was introduced in the chamber and used to put in close proximity aggregates with similar sizes to facilitate the fusion. 2D fusion time-lapses were acquired in transmission at 0.2 fps for 2 minutes. To characterize the fusion dynamics, the temporal evolution of the contact surface between aggregates was quantitated via kymographs.

Wetting of bacterial aggregates

Glass substrates of CellView cell culture slides (Greiner, REF. 543979) were plasma activated and coated with 100 µg/ml FITC-conjugated lectin from *Triticum Vulgaris* (Sigma-Aldrich, L4895) to allow bacterial adhesion. Bacterial aggregates from a 2h pre-culture in RPMI + 10% FBS were loaded and fast time-lapse acquisition in TIRF mode was started to selectively visualize the temporal evolution of the aggregate contact area with the substrate over 20 minutes.

Micropipette aspiration

Micropipette aspiration was largely performed as previously described (Guevorkian et al., 2010). Pipettes were fabricated by pulling borosilicate capillaries (1mm/0.78mm O/I diameter, Harvard Apparatus) with a laser-based puller (P-2000, Sutter Instruments). and sized to the desired diameter and fire-polished by using a microforge with a heated glass ball, to generate a smooth glass surface. Finally, the pipette tip was slightly bent by heating it with a flame, in order to minimize the angle between the pipette and the bottom of the

observation chamber. A liquid suspension of bacterial aggregates was transferred to a tissue culture treated plastic Ibidi µ-dish (Biovalley, France) with walls cut to facilitate the access of the micropipette. Aggregates were then suspended in 600 µl of RPMI + 10% FBS and the open end was sealed with mineral oil to prevent evaporation. The micropipette was eventually introduced into the chamber. A range of pressures (ΔP = 10-100 Pa) was attained by vertically displacing a water reservoir, connected to the pipette, with respect to the observation chamber. Movies of the progression of aggregates inside the pipette were recorded in bright field with a frame rate of 10 images/s. Image processing was performed using Image J software (Schneider et al., 2012).

Live-cell imaging

Acquisitions were performed on a Ti-inverted spinning disk microscope (Nikon) at 37°C, with 5% CO_2 atmosphere, using 20X (NA 0.75), 40X (NA 1.3) and 100X (NA 0.5-1.3) objectives. Images were acquired using Metamorph (Molecular Devices). The excitation source was either transmission illumination or the 491, 561, 642 laser line. Images were acquired with a EMCCD camera (Evolve, Photometrics). TIRF images were acquired with an ORCA C8484-03G01 Hamamatsu camera.

Single bacteria tracking in aggregates and analysis

Plastic bottom microchannels (Ibidi) were passivated upon plasma activation and 30 min incubation with 0.1 mg/ml PLL(20)-g[3.5]-PEG(2) (Surface Solutions) solution in 10mM HEPES pH 7.4. Bacteria from 2h pre-cultures in RPMI + 10% FBS and various concentrations of IPTG if needed, were then loaded in microchannels (Ibidi) and allowed to settle for 15 minutes at 37°C. Streaming movies of 10-20 s (time frame 30 ms) of iRFP expressing bacteria were acquired with a 100X objective at the confocal middle plane using aggregates of similar sizes (30-40 µm in diameter) for the different conditions. Movies were post-processed with a standardized protocol on Fiji software, comprising background subtraction, Gaussian blurring and masking to define the aggregate contour. Single bacteria

tracking was performed also on Fiji with Trackmate plugin. Analysis of bacterial tracks was performed with a custom-built script in Matlab: briefly, average distance from the aggregate center of mass and mean square displacements (MSD) were calculated over each single bacterial track. Diffusion coefficients were extracted with a linear fit on the initial portion (10%) of the MSD curve. Aggregate size was normalized to 1 in order to obtain a cumulative distribution of diffusion coefficients over multiple aggregates (n=20). Data were binned to extract average values and corresponding standard deviations in different aggregate regions.

Micro-chambers fabrication

Masters containing round micropillars of different sizes were fabricated using conventional positive photolithography techniques. The designs of the brass master molds were created using Clewin software. Briefly, a silicon wafer (Neyco S.A. France; diameter = 4-inch, thickness = 525) was spin-coated with TI Prime adhesion promoter (Microchemicals) and resist AZ® 9260 (Microchemicals). Predesigned features were patterned through a mask aligner (MJB4, Süss Microtec ReMan GmbH, Germany) equipped with an I-Liner filter (365nm) and a chuck for 4-inch wafers. The non-exposed resist was removed by solvent AZ® 400K in water solution, air dried and passivated by overnight exposure to Trichloro(1H,1H,2H,2H-perfluorooctyl)silane vapors (Sigma Aldrich, ref: 448931). A 10:1 mixture of PDMS Sylgard 184 or RTV614 silicone elastomer and curing agent was poured onto the brass master and cured at 65°C for 3 h. PMDS chips were cleaned with isopropanol before a 30-s exposure to air plasma for activation. Agarose micro-chambers were prepared by pouring molten 2% agarose containing FITC-Dextran (MW 15 kD; Life Technologies) onto the PDMS chip. The agar pad was then stripped off, flipped and resized to a final 5 mm X 5 mm thick pad. Cells at OD600~0.3 were diluted 20-fold, and 2 µL of bacterial suspension were loaded onto the agarose pad. As soon as the agar surface appeared dry, the pad was flipped onto a plastic bottom Fluorodish (Ibidi) previously passivated upon plasma activation and 30 min incubation with 0.1 mg/ml PLL(20)-g[3.5]-PEG(2) (Surface Solutions) solution in

10mM HEPES pH 7.4. Streaming movies of single iRFP-expressing WT bacteria diffusing in the micro-chambers were acquired with a 40X objective at 200ms time frame for 3-5 minutes.

Analysis of bacterial interactions

Single bacteria tracking was performed on Fiji with Trackmate plug-in and post-processed with a custom-made Matlab script. We defined the 2 states of interactions between bacterial pairs as follows: (i) Attraction phase (or ON): this combines the active period where cells approach towards each other in a highly ballistic manner with a high speed, and the following contact period where bacteria remain in close proximity (cell-cell distance below threshold of 3 μm); (ii) No interaction phase (or OFF): corresponds to the time period where bacteria do not interact, e.g. they diffuse freely and are not in close proximity (cell-cell above threshold of 3 μm).

The approach phase was defined by characterizing the time-evolution of cell-cell distance as follows. First, we compute the relative cell-cell position $\vec{X}_3(t)$ and distance $L(t)$ as:

$$\vec{X}_3(t) = \vec{X}_1(t) - \vec{X}_2(t)$$

$$L(t) = \left|\vec{X}_3(t)\right|$$

where $\vec{X}_1(t)$ and $\vec{X}_2(t)$ denote the 2D positions at instant t of bacterium 1 and 2 respectively. Their time derivatives, relative velocity $\vec{V}(t)$ and rate of distance change $\dot{L}(t)$, were defined as:

$$\vec{V}(t) = \frac{\left(\vec{X}_3(t+\tau/2) - \vec{X}_3(t-\tau/2)\right)}{\tau}$$

$$\dot{L}(t) = \frac{\left(L(t+\tau/2) - L(t-\tau/2)\right)}{\tau}$$

where τ = 6 frames = 1.2 s.

The approach phases are characterized by a fast, ballistic approach of two bacteria, where cell-cell relative distance decreases rapidly. These phases were automatically detected by adopting two criteria:

(1) Approach phases correspond to a sharp decrease of $\dot{L}(t)$ to large negative values followed by its increase back to ~ 0; therefore, they should contain a local minimum of $\dot{L}(t)$.

(2) $\dot{L}(t)$ at the local minimum should be smaller than a threshold value, $Thr1$. $Thr1$ was set to be -2.5 μm/s. This principle is necessary to distinguish true approach phases from other random non-directed motions.

The beginning and the end of a single approach phase were defined as the time points where $\dot{L}(t)$ exceeds a second threshold $Thr2$. $Thr2$ was set to be -1 μm/s.

The approach dynamics was characterized by computing the approach speed and orientation. The approach speed was defined as the norm of relative velocity:

$$\vec{V}_{INT}(t) = \left|\vec{V}(t)\right|$$

The approach orientation θ_{INT} was defined as the orientation of $\left|\vec{V}(t)\right|$:

$$\theta_{INT} = tan^{-1}\left(\vec{V}(t) - \vec{X}_3(t)\right)$$

Note that if two bacteria are approaching straightly, θ_{INT} is 0 and approach speed is equal to $\dot{L}(t)$. Average speed and velocity orientation were defined as temporal averages for the entire period. Finally, analyses of all interaction events between bacterial pairs were pulled together to generate probability distributions of each parameter. Mean values of interaction distance, time of interaction (t_{ON}) and time of non-interaction (t_{OFF}) were derived by exponential fits, while mean values of interaction speed and interaction angle were derived by Gaussian fits.

Notations:

$\vec{X}_1(t)$, $\vec{X}_2(t)$: 2D position of bacteria 1 and 2 at time x_1, vector

$\vec{X}_3(t)$: relative position of x_1 and x_2, vector

$L(t)$: relative distance between two bacteria, scalar

$\vec{V}(t)$: relative true speed

$\dot{L}(t)$: change rate of $L(t)$ = projection of $\vec{V}(t)$ for cell-cell axis

Microchannels experiment

Microchannels were a kind gift from Matthieu Piel's lab, and were prepared as previously described(Heuze et al., 2011). Briefly, a 10:1 mixture of PDMS Sylgard 184 or RTV614 silicone elastomer and curing agent was poured onto the epoxy replica and cured at 65°C for 3h, to prepare microchannels of different sizes (12 µm X 8 µm, 5 µm X 4 µm). Channel inlets were punched with a 2.5-mm puncher before bonding. The PDMS chamber and an Ibidi µ-slide 2 well with glass-bottom dish (80287, Biovalley) were exposed to 45 s oxygen plasma for bonding. The binding was left to strengthen in a 65 °C oven for 1 h. Finally, chambers were exposed for 10 min to UV light for sterilization (UVO cleaner, Jelight), and incubated with RPMI + 10% FBS for at least 1 h at 37 °C and 5% CO_2 before cell loading. Bacteria from 2 hs pre-cultures in the same medium were re-suspended at a final OD 0.1, vortexed and then injected in the chamber. Finally, the chamber was immersed in medium to prevent evaporation. Time-lapse microscopy was performed in parallel on WT and *pilT* strains in two separated wells over 10h and temporal evolution of aggregate size was quantified.

References:

Biais, N., Ladoux, B., Higashi, D., So, M., and Sheetz, M. (2008). Cooperative retraction of bundled type IV pili enables nanonewton force generation. PLoS Biol *6*, e87.

573 Brissac, T., Mikaty, G., Dumenil, G., Coureuil, M., and Nassif, X. (2012). The meningococcal
574 minor pilin PilX is responsible for type IV pilus conformational changes associated with
575 signaling to endothelial cells. Infect Immun *80*, 3297-3306.
576 Budrene, E.O., and Berg, H.C. (1991). Complex patterns formed by motile cells of
577 Escherichia coli. Nature *349*, 630-633.
578 Filonov, G.S., Piatkevich, K.D., Ting, L.M., Zhang, J., Kim, K., and Verkhusha, V.V. (2011).
579 Bright and stable near-infrared fluorescent protein for in vivo imaging. Nat Biotechnol *29*,
580 757-761.
581 Guevorkian, K., Colbert, M.J., Durth, M., Dufour, S., and Brochard-Wyart, F. (2010).
582 Aspiration of biological viscoelastic drops. Phys Rev Lett *104*, 218101.
583 Guevorkian, K., Gonzalez-Rodriguez, D., Carlier, C., Dufour, S., and Brochard-Wyart, F.
584 (2011). Mechanosensitive shivering of model tissues under controlled aspiration. Proc Natl
585 Acad Sci U S A *108*, 13387-13392.
586 Heuze, M.L., Collin, O., Terriac, E., Lennon-Dumenil, A.M., and Piel, M. (2011). Cell
587 migration in confinement: a micro-channel-based assay. Methods Mol Biol *769*, 415-434.
588 Imhaus, A.F., and Dumenil, G. (2014). The number of Neisseria meningitidis type IV pili
589 determines host cell interaction. EMBO J *33*, 1767-1783.
590 Maier, B., Potter, L., So, M., Long, C.D., Seifert, H.S., and Sheetz, M.P. (2002). Single pilus
591 motor forces exceed 100 pN. Proc Natl Acad Sci U S A *99*, 16012-16017.
592 Mairey, E., Genovesio, A., Donnadieu, E., Bernard, C., Jaubert, F., Pinard, E., Seylaz, J.,
593 Olivo-Marin, J.C., Nassif, X., and Dumenil, G. (2006). Cerebral microcirculation shear stress
594 levels determine Neisseria meningitidis attachment sites along the blood-brain barrier. J Exp
595 Med *203*, 1939-1950.
596 Marathe, R., Meel, C., Schmidt, N.C., Dewenter, L., Kurre, R., Greune, L., Schmidt, M.A.,
597 Muller, M.J., Lipowsky, R., Maier, B.*, et al.* (2014). Bacterial twitching motility is coordinated
598 by a two-dimensional tug-of-war with directional memory. Nat Commun *5*, 3759.

599 Melican, K., Michea Veloso, P., Martin, T., Bruneval, P., and Dumenil, G. (2013). Adhesion
600 of Neisseria meningitidis to dermal vessels leads to local vascular damage and purpura in a
601 humanized mouse model. PLoS Pathog *9*, e1003139.
602 Merz, A.J., So, M., and Sheetz, M.P. (2000). Pilus retraction powers bacterial twitching
603 motility. Nature *407*, 98-102.
604 Nassif, X., Lowy, J., Stenberg, P., O'Gaora, P., Ganji, A., and So, M. (1993). Antigenic
605 variation of pilin regulates adhesion of Neisseria meningitidis to human epithelial cells. Mol
606 Microbiol *8*, 719-725.
607 Oldewurtel, E.R., Kouzel, N., Dewenter, L., Henseler, K., and Maier, B. (2015). Differential
608 interaction forces govern bacterial sorting in early biofilms. Elife *4*.
609 Persat, A., Nadell, C.D., Kim, M.K., Ingremeau, F., Siryaporn, A., Drescher, K., Wingreen,
610 N.S., Bassler, B.L., Gitai, Z., and Stone, H.A. (2015). The mechanical world of bacteria. Cell
611 *161*, 988-997.
612 Pujol, C., Eugene, E., Marceau, M., and Nassif, X. (1999). The meningococcal PilT protein is
613 required for induction of intimate attachment to epithelial cells following pilus-mediated
614 adhesion. Proc Natl Acad Sci U S A *96*, 4017-4022.
615 Rotman, E., and Seifert, H.S. (2014). The genetics of Neisseria species. Annu Rev Genet
616 *48*, 405-431.
617 Rusniok, C., Vallenet, D., Floquet, S., Ewles, H., Mouze-Soulama, C., Brown, D., Lajus, A.,
618 Buchrieser, C., Medigue, C., Glaser, P.*, et al.* (2009). NeMeSys: a biological resource for
619 narrowing the gap between sequence and function in the human pathogen Neisseria
620 meningitidis. Genome Biol *10*, R110.
621 Schneider, C.A., Rasband, W.S., and Eliceiri, K.W. (2012). NIH Image to ImageJ: 25 years
622 of image analysis. Nat Methods *9*, 671-675.
623 Taktikos, J., Lin, Y.T., Stark, H., Biais, N., and Zaburdaev, V. (2015). Pili-Induced Clustering
624 of N. gonorrhoeae Bacteria. PLoS One *10*, e0137661.
625 Weber, C.A., Lin, Y.T., Biais, N., and Zaburdaev, V. (2015). Formation and dissolution of
626 bacterial colonies. Phys Rev E Stat Nonlin Soft Matter Phys *92*, 032704.

Supplementary Materials contain:

SI Model

Table T1

Figures S1-S5

Movies S1-S8

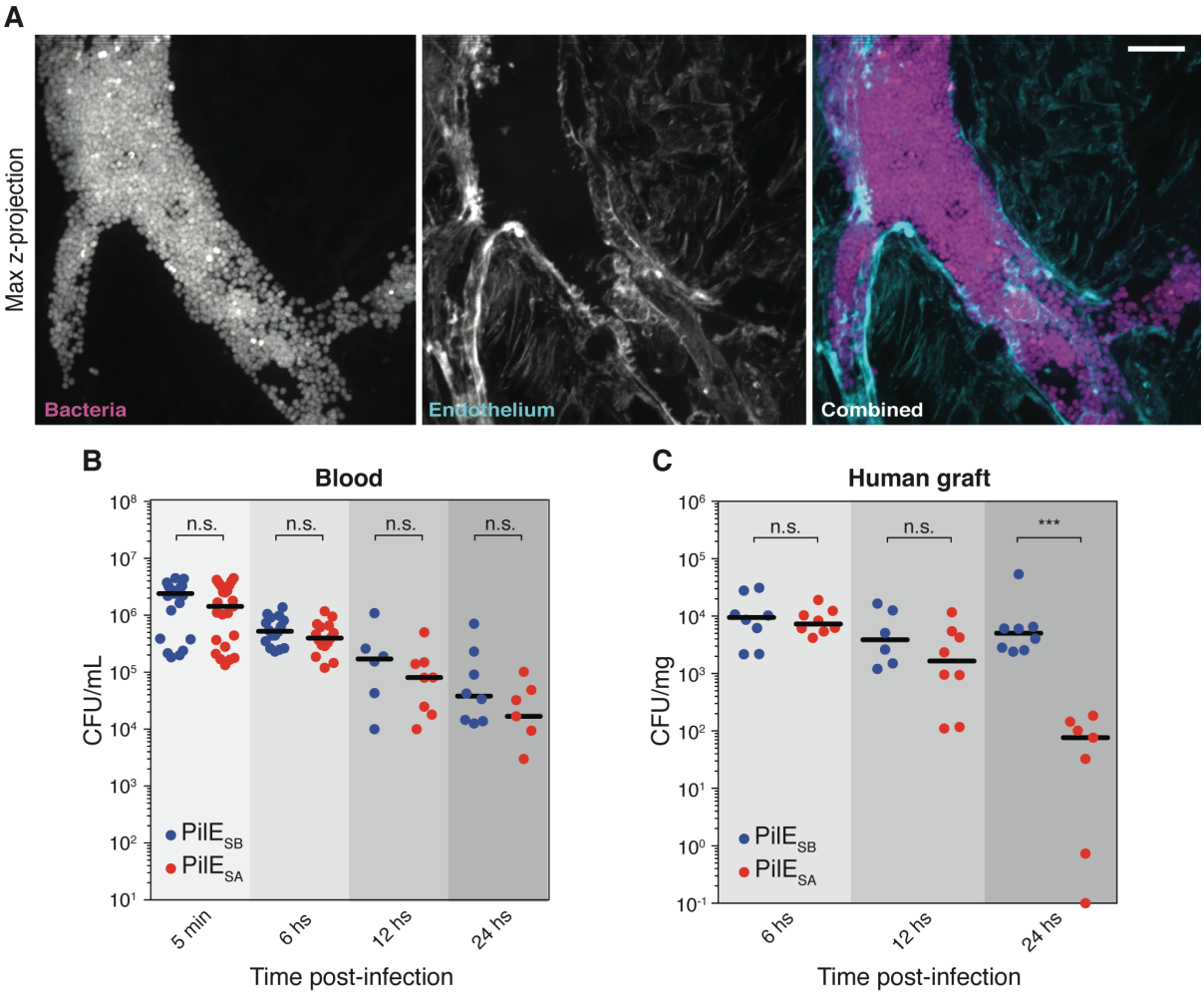
A
Max z-projection
Bacteria
Endothelium
Combined
B
Blood
CFU/mL
n.s.
n.s.
n.s.
n.s.
PilE_SB
PilE_SA
5 min
6 hs
12 hs
24 hs
Time post-infection
C
Human graft
CFU/mg
n.s.
n.s.
***
PilE_SB
PilE_SA
6 hs
12 hs
24 hs
Time post-infection

Fig. 1

Figure 1: Bacterial auto-aggregation enhances vascular colonization *in vivo*. (A) Maximal z-projection from confocal slices of an infected vessel at 6h post-infection in a xenograft model of infection showing the human endothelium surface (Rhodamin-labelled Ulex Europeus Agglutinin), GFP-expressing *Neisseria meningitidis* aggregates and corresponding merged image. Scale bar, 10 µm. **(B)** Bacterial colony forming unit (CFU) counts from the blood of mice grafted with human skin and infected with the *N. meningitidis* pilin variants $PilE_{SB}$ (indicated in blue) and $PilE_{SA}$ (indicated in red). These counts represent the number of bacteria circulating in the blood at a given time-point. **(C)** Bacterial CFU counts from skin biopsies taken from grafted human skin of mice infected with the *N. meningitidis* pilin variants $PilE_{SB}$ (indicated in blue) and $PilE_{SA}$ (indicated in red). These counts indicated the number of bacteria attached to the capillary endothelium at a given time point. Each data point represents one infected mice. Black bars indicate average values for each condition. n.s. = not significant; ***: P-value = 0.0003.

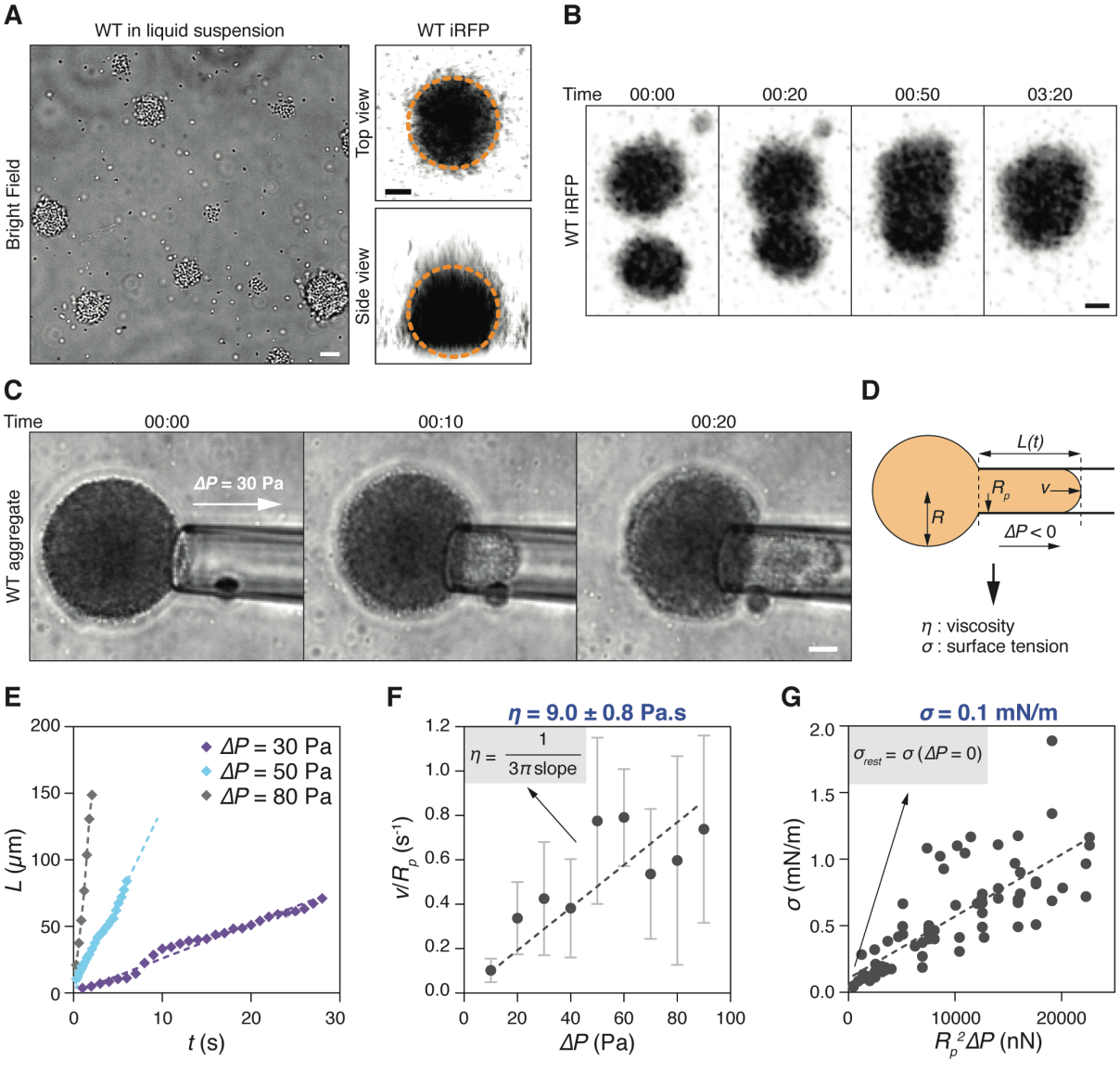
A
WT in liquid suspension
WT iRFP
Bright Field
Top view
Side view
B
Time
00:00
00:20
00:50
03:20
WT iRFP
C
Time
00:00
00:10
00:20
WT aggregate
ΔP = 30 Pa
D
L(t)
R
R_p
v
ΔP < 0
η : viscosity
σ : surface tension
E
ΔP = 30 Pa
ΔP = 50 Pa
ΔP = 80 Pa
L (μm)
t (s)
F
η = 9.0 ± 0.8 Pa.s
η = 1 / 3π slope
v/R_p (s^-1)
ΔP (Pa)
G
σ = 0.1 mN/m
σ_rest = σ (ΔP = 0)
σ (mN/m)
R_p^2 ΔP (nN)

Fig. 2

Figure 2: *Neisseria meningitidis* aggregates display a viscous liquid behavior in suspension. (A) On the left, Bright-Field image of WT bacterial aggregates. On the right, top and side confocal views of a WT iRFP bacterial aggregate. The quasi-spherical aggregate shape in both views is highlighted by a dotted orange line. The plastic substrate was treated with PLL-PEG to minimize adhesion events. Scale bars, 10 μm. **(B)** Confocal time-lapse of a fusion event between WT iRFP bacterial aggregates. Indicated times are in min:sec. Scale bar, 10 μm. **(C)** Bright-field temporal evolution of a WT aggregate progressing into a micropipette upon aspiration (ΔP = 30 Pa). Indicated times are in min:sec. Scale bar, 10 μm. **(D)** Schematic representation of micropipette aspiration and definition of physical parameters to estimate aggregate viscosity and surface tension. R: aggregate radius; R_p: pipette radius; $L(t)$: tongue length at instant t; ΔP: applied negative pressure; v: tongue progression speed in the pipette; η: aggregate viscosity; σ: aggregate surface tension. **(E)** Aggregate progression inside the pipette (tongue length, L) as a function of time t upon application of 3 different pressures: 30, 50 and 80 Pa, indicated with violet, light blue and grey dots respectively. Dotted lines indicate corresponding linear fits used to estimate tongue progression speed. **(F)** Tongue progression speed to pipette radius ratios for a range of applied pressures (10-100 Pa). Dots and error bars indicate corresponding average values and standard deviations for each applied pressure, ΔP. N=80 WT aggregates. A linear fit to extract aggregate viscosity is represented by a dotted line. **(G)** Surface tension as a function of the applied force $R_p^2 \Delta P$. Dots indicate single surface tension estimations for each aspiration event. Surface tension at rest is extrapolated with a linear fit (dotted line) at corresponding null force. N=80 WT aggregates.

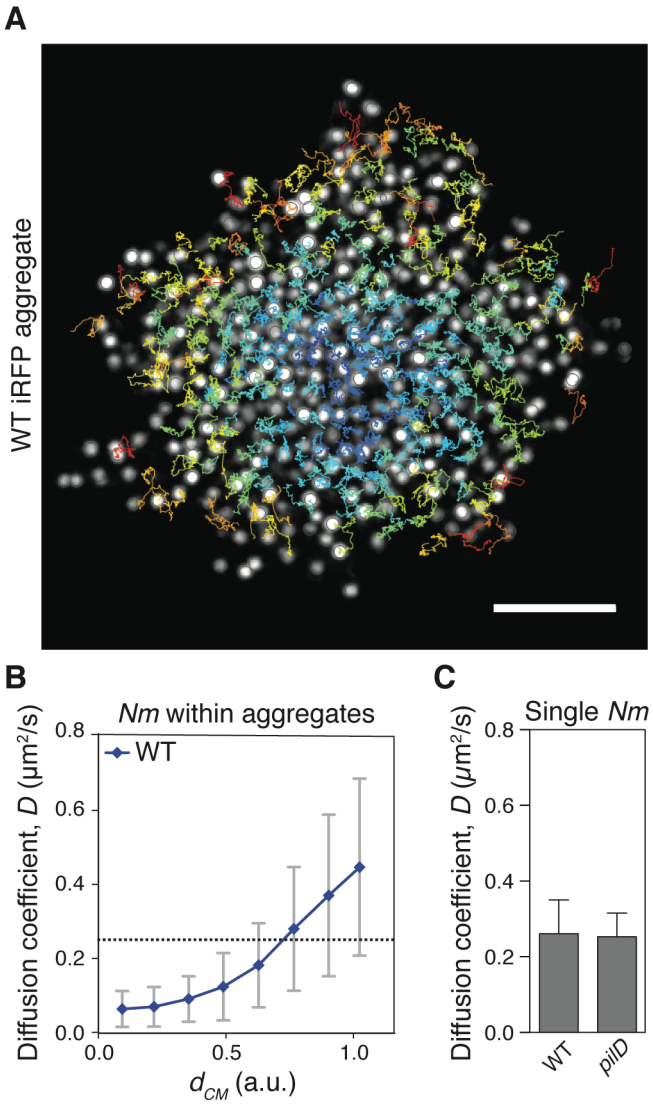
A
WT iRFP aggregate
B
Nm within aggregates
WT
Diffusion coefficient, D (μm²/s)
0.0
0.2
0.4
0.6
0.8
0.0
0.5
1.0
d_CM (a.u.)
C
Single Nm
Diffusion coefficient, D (μm²/s)
WT
pilD

Fig. 3

Figure 3: Diffusion of bacteria inside the aggregates reaches values higher than individual bacteria in suspension. (A) Single confocal slice of a WT iRFP aggregate in the middle plane, and overlay of single bacterial tracks over a 10 s period with 30 ms time step. Tracks are color-coded depending on their mean instantaneous speeds. Scale bar, 10 μm. **(B)** Average effective diffusion coefficients and corresponding standard deviations of individual bacteria as a function of their normalized distance from the aggregate center of mass, d_{CM} (0, center; 1; periphery). N=20 WT aggregates of similar size. Dotted line indicates the average diffusion coefficient of individual isolated WT bacteria. **(C)** Average diffusion coefficients and corresponding standard deviations of individual bacteria for WT and the non-piliated mutant *pilD*.

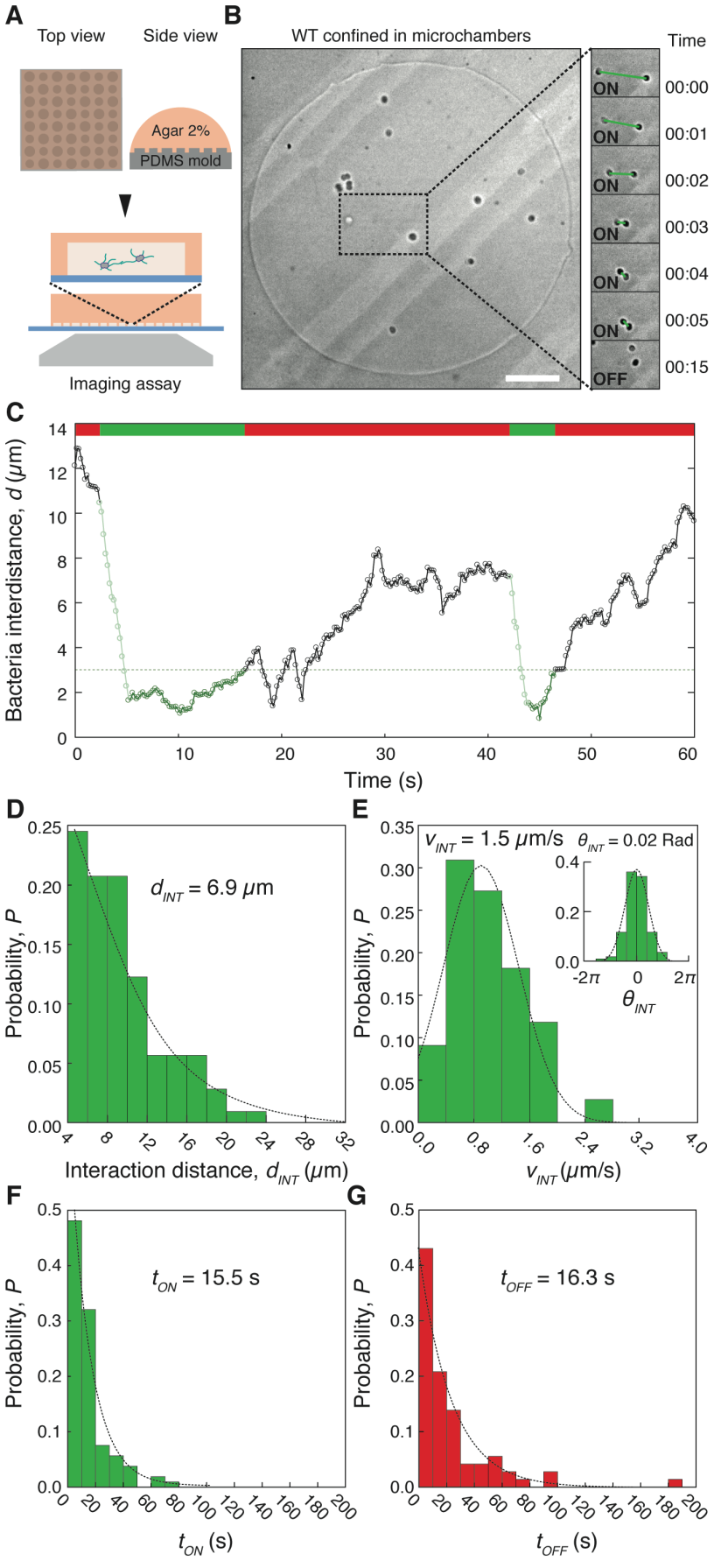
A
Top view
Side view
Agar 2%
PDMS mold
Imaging assay
B
WT confined in microchambers
Time
ON
00:00
ON
00:01
ON
00:02
ON
00:03
ON
00:04
ON
00:05
OFF
00:15
C
Bacteria interdistance, d (μm)
Time (s)
D
Probability, P
d_{INT} = 6.9 μm
Interaction distance, d_{INT} (μm)
E
v_{INT} = 1.5 μm/s
θ_{INT} = 0.02 Rad
Probability, P
v_{INT} (μm/s)
θ_{INT}
F
Probability, P
t_{ON} = 15.5 s
t_{ON} (s)
G
Probability, P
t_{OFF} = 16.3 s
t_{OFF} (s)

Fig. 4

Figure 4: Pairwise interaction between bacteria shows cycles of attraction and release. (A) Schematic of agar chamber fabrication and experimental setup to observe the interaction of a controlled number of bacteria. **(B)** On the left, Bright-field view of WT bacteria confined inside agar chambers. On the right, zoom-in view of a time-lapse sequence showing an event of attraction (indicated by a green line) and release between two bacteria. Time is indicated in min:sec. **(C)** Interbacterial distance measured as a function of time for the pair highlighted in Figure 3B. The attraction and contact phases appear in light and dark green respectively, while the non-interacting phases appear in red. An arbitrary threshold of 3 μm for the interbacterial distance was chosen to define the end of the ON phase. **(D)** Probability distribution histogram of measured interaction distances. A mean value is extracted with an exponential fit. **(E)** Probability distribution histogram of measured approaching speeds and angles (inset). Mean values are extracted with a gaussian fit. **(F)** Probability distribution histogram of measured interaction times (t_{ON}). A mean value is extracted with an exponential fit. (**G**) Probability distribution histogram of measured non-interacting time while within interaction range (t_{OFF}). A mean value is extracted with an exponential fit.

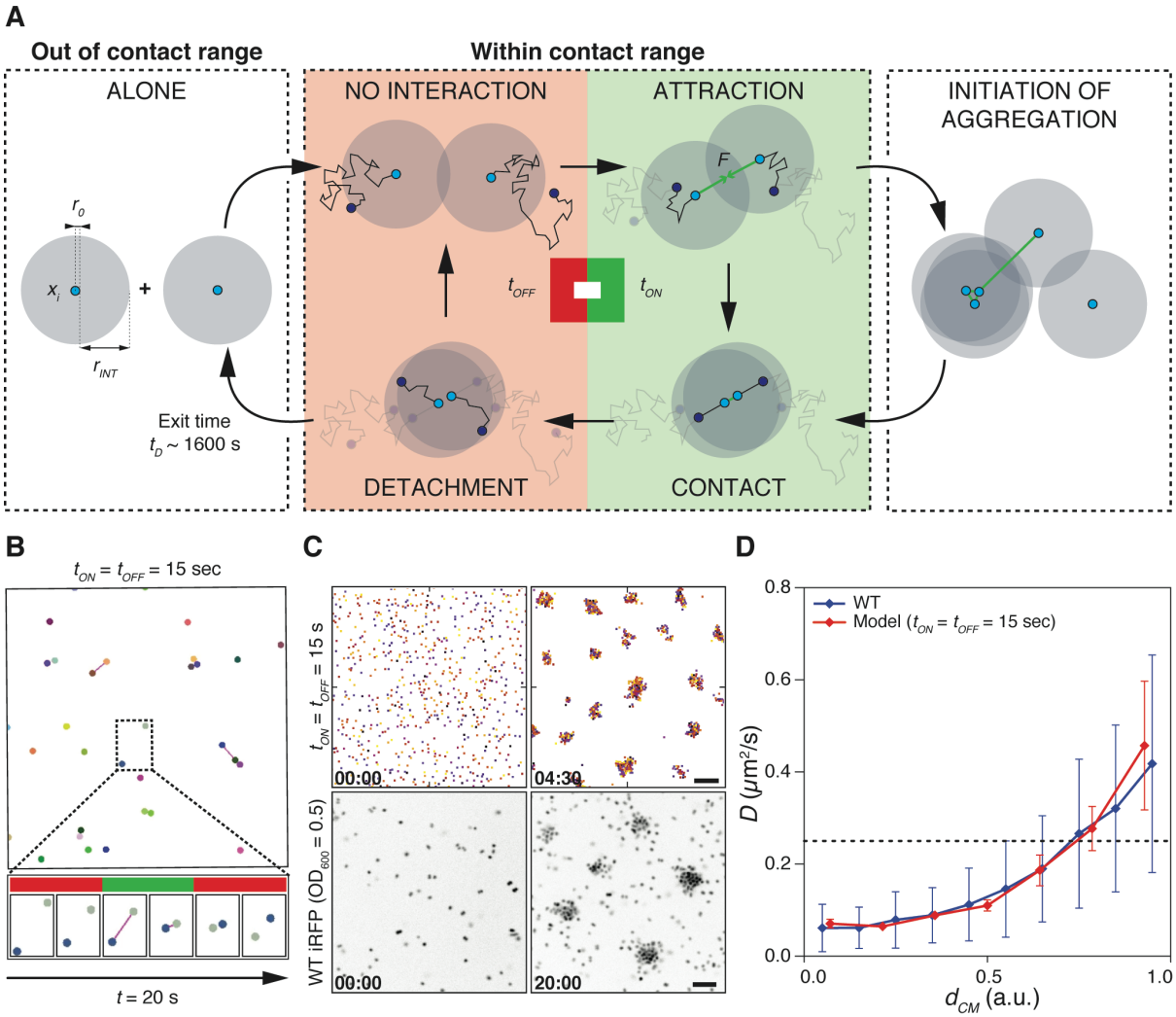
A
Out of contact range
Within contact range
ALONE
NO INTERACTION
ATTRACTION
INITIATION OF AGGREGATION
r_0
x_i
+
r_{INT}
Exit time
t_D ~ 1600 s
F
t_{OFF}
t_{ON}
DETACHMENT
CONTACT
B
$t_{ON} = t_{OFF}$ = 15 sec
t = 20 s
C
$t_{ON} = t_{OFF}$ = 15 s
WT iRFP (OD_{600} = 0.5)
00:00
04:30
00:00
20:00
D
WT
Model ($t_{ON} = t_{OFF}$ = 15 sec)
D (μm^2/s)
d_{CM} (a.u.)
0.0
0.2
0.4
0.6
0.8
0.0
0.5
1.0

Fig. 5

Figure 5: An intermittent attractive force between particle pairs is sufficient to recapitulate aggregate properties. (A) Schematic of the main physical principles implemented in the computational model of intermittent interaction. Individual particles are defined by a hard core (r_0) and an interaction range (r_{INT}). When the pair is within the interaction distance r_{INT}, it has a given probability of interaction (t_{ON}). During the interaction phase, an equal attractive force (F) is exerted on both particles bringing them together and keeping them in contact; finally, the force is released, particles detach and move away from each other. The exit time t_D corresponds to the time necessary for two particles to be out of range after contact by diffusion only. In the case of bacteria, $t_D \sim 1600$ s considering $D = 0.25$ $\mu m^2/s$ and a 20 µm maximum contact range. **(B)** On the top, view of simulated interactions between particles for $t_{ON} = t_{OFF} = 15$ s. On the bottom, zoom-in view on a simulated time-lapse showing interacting and non-interacting phases between two particles over 20 s, indicated in green and red respectively. **(C)** On the top, simulation of aggregate formation dynamics starting from an initial random distribution, for $t_{ON} = t_{OFF} = 15$ s and high particle density. On the bottom, aggregate formation dynamics of WT iRFP bacteria at $OD_{600} = 0.5$. Time is indicated in min:sec. Scale bars, 10 µm. **(D)** *In vitro* and *in silico* effective diffusion coefficients of individual bacteria inside WT aggregates as a function of normalized distance from the aggregate center of mass (d_{CM}), indicated in blue and red respectively. Simulated aggregates correspond to $t_{ON} = t_{OFF} = 15$ s. Dots and error bars correspond to average values and standard deviations. The dotted line indicates the experimentally determined diffusion coefficient of isolated bacteria.

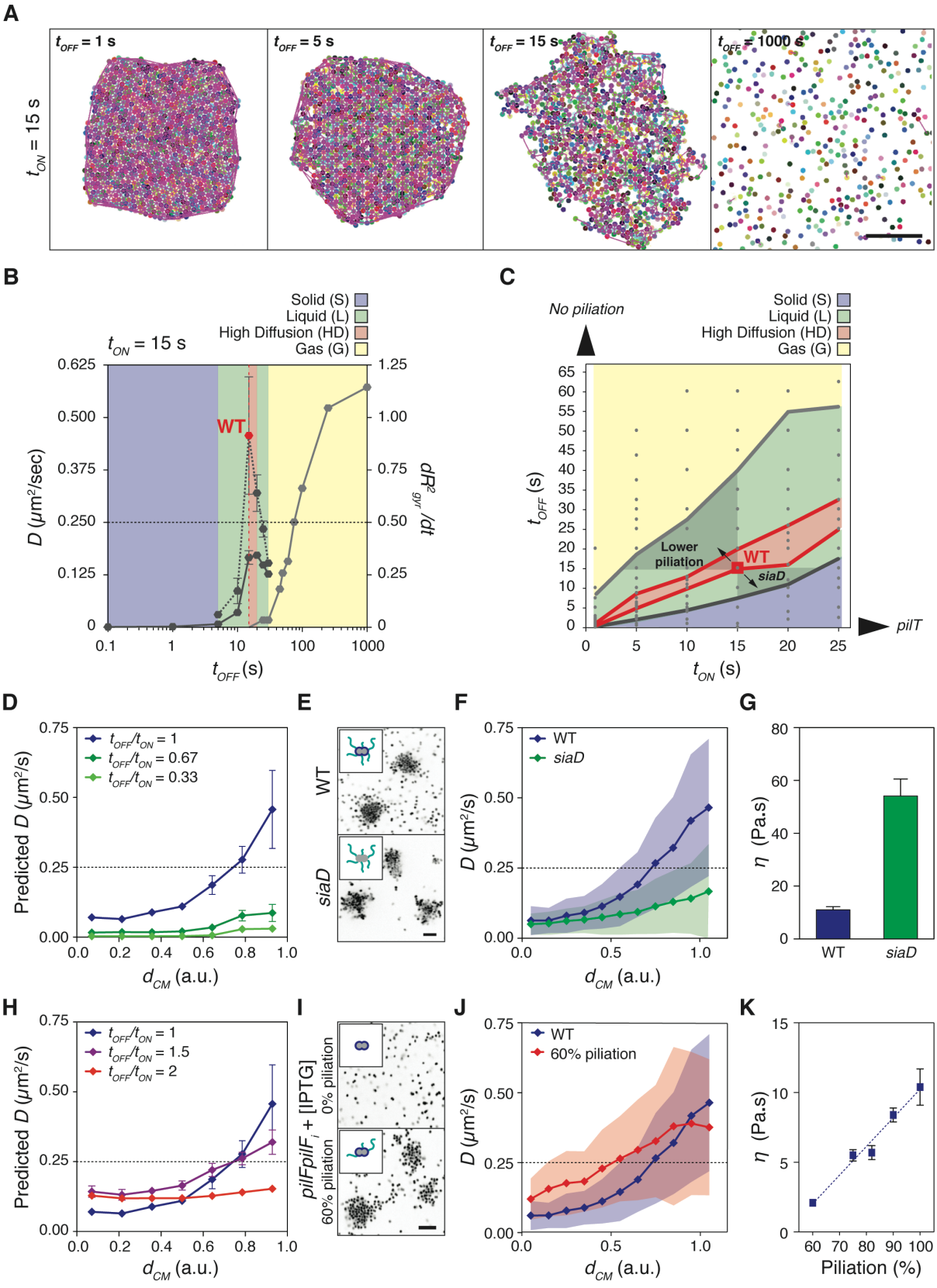
A
t_{OFF} = 1 s
t_{OFF} = 5 s
t_{OFF} = 15 s
t_{OFF} = 1000 s
t_{ON} = 15 s
B
Solid (S)
Liquid (L)
High Diffusion (HD)
Gas (G)
t_{ON} = 15 s
WT
D (μm²/sec)
dR^2_{gyr}/dt
t_{OFF} (s)
C
No piliation
Solid (S)
Liquid (L)
High Diffusion (HD)
Gas (G)
t_{OFF} (s)
Lower piliation
WT
siaD
pilT
t_{ON} (s)
D
Predicted D (μm²/s)
t_{OFF}/t_{ON} = 1
t_{OFF}/t_{ON} = 0.67
t_{OFF}/t_{ON} = 0.33
d_{CM} (a.u.)
E
WT
siaD
F
WT
siaD
D (μm²/s)
d_{CM} (a.u.)
G
η (Pa.s)
WT
siaD
H
Predicted D (μm²/s)
t_{OFF}/t_{ON} = 1
t_{OFF}/t_{ON} = 1.5
t_{OFF}/t_{ON} = 2
d_{CM} (a.u.)
I
pilFpilF$_i$ + [IPTG]
0% piliation
60% piliation
J
WT
60% piliation
D (μm²/s)
d_{CM} (a.u.)
K
η (Pa.s)
Piliation (%)

Fig. 6

Figure 6: Intermittent attractive properties between bacteria define a phase diagram of aggregation phenotypes. (A) Views of *in silico* aggregation states for a fixed value of t_{ON} = 15 s and four different values of t_{OFF}: 1, 5, 15 and 1000 seconds. Scale bar, 10 μm. **(B)** Theoretical phase diagram of particle behavior as a function of t_{OFF} for a fixed value of t_{ON} = 15 s. Solid (blue) to liquid (green) transition is defined with the average diffusion coefficient of all particles in the aggregate (left axis, dark grey line). Liquid (green) to gas (yellow) transition is defined with the aggregate expansion rate, calculated as the derivative of square gyration radius (right axis, light grey line). The high diffusion zone (red) corresponds to a regime where the average diffusion coefficient of particles at the aggregate periphery (left axis, dark grey dotted line) exceeds the diffusion coefficient of isolated bacteria (black dotted line). Location of WT bacterial aggregates is indicated with a red dot and red dotted line. **(C)** Theoretical phase diagram of particle behavior as a function of t_{ON} and t_{OFF}. The color code is the same as in 4B. Grey dots indicate all simulated conditions to assess phase transitions. Light grey regions illustrate model predictions for lower (bottom right region, corresponding to *siaD* mutant) or higher (top left region, corresponding to underpiliated mutants) t_{OFF}/t_{ON} ratios. Non-piliated mutants are located at the extreme top left of the diagram, corresponding to infinite t_{OFF}/t_{ON} ratio. Hyperpiliated mutant with non-retractile T4P (*pilT*) is located at the extreme bottom right of the diagram, corresponding to null t_{OFF}/t_{ON} ratio. **(D)** Simulated diffusion coefficient as a function of the position in the aggregate with decreasing t_{OFF}/t_{ON} ratios (1, 0.67 and 0.33). **(E)** On the top left, schematic of WT and non-capsulated *siaD* mutant. On the right, corresponding views of iRFP-expressing aggregates for each strain. Scale bar, 10 μm. **(F)** Experimental measurement of the diffusion coefficient of individual bacteria as a function of their positon in the aggregate for WT (blue) and *siaD* (green). Average values and corresponding standard deviations are indicated with dots and filled regions respectively. **(G)** Viscosity of the *siaD* (green) mutant compared to WT (blue) as determined by micropipette aspiration. **(H)** Simulated diffusion coefficient as a function of the position in the aggregate with increasing t_{OFF}/t_{ON} ratios (1, 1.5 and 2). **(I)** On the top left, schematic of the *pilF* inducible strain with amounts of inducer generating 0% (top) and 60%

(bottom) of piliation relative to WT. On the right, corresponding view of iRFP-expressing bacteria for each condition. Scale bar, 10 μm. **(J)** Experimental measurement of the diffusion coefficient of individual bacteria as a function of their positon in the aggregate for WT (blue) and *pilF* inducible strain at 60% of piliation (red). Average values and corresponding standard deviations are indicated with dots and filled regions respectively. **(K)** Viscosity of the *pilF* inducible strain treated with various levels of inducer and thus different levels of piliation as determined by micropipette aspiration.

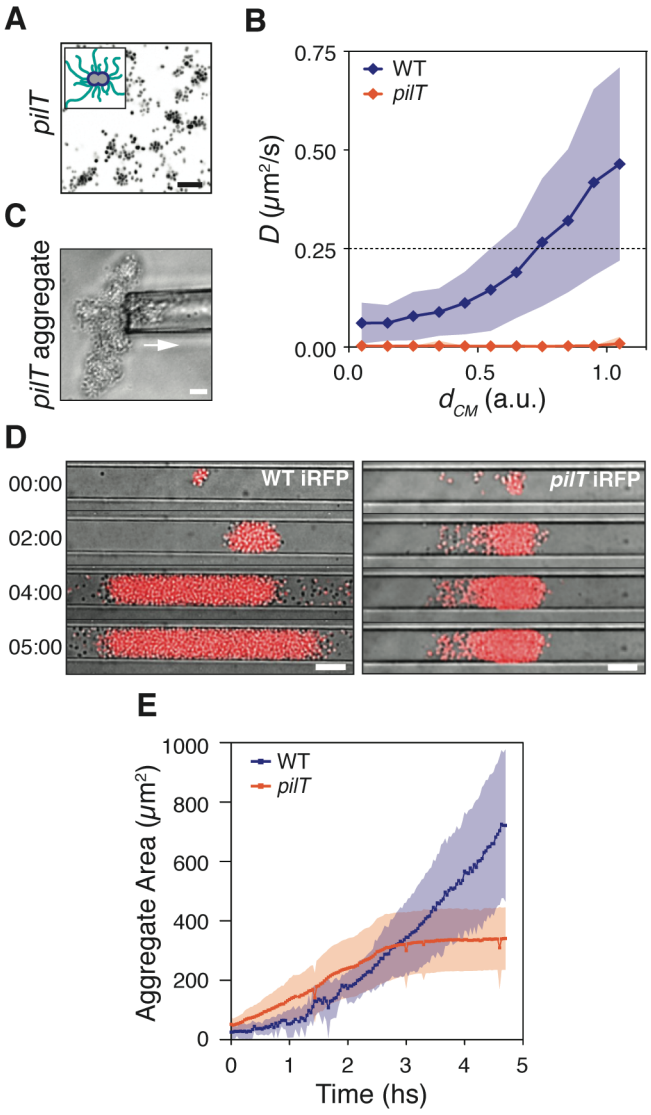
A
pilT
B
0.75
0.50
0.25
0.00
WT
pilT
D (μm²/s)
0.0
0.5
1.0
d_CM (a.u.)
C
pilT aggregate
D
00:00
02:00
04:00
05:00
WT iRFP
pilT iRFP
E
1000
800
600
400
200
0
Aggregate Area (μm²)
WT
pilT
0
1
2
3
4
5
Time (hs)

Fig. 7

750

Figure 7: Fluid-like behavior of aggregates favors colonization of capillary mimics. (A) Schematic of the *pilT* mutant and corresponding view of iRFP-expressing mutant aggregates. Scale bar, 10 μm. **(B)** Experimental measurement of the diffusion coefficient of individual bacteria as a function of their positon in the aggregate for WT (blue) and *pilT* (orange). Average values and corresponding standard deviations are indicated with dots and filled regions respectively. **(C)** Bright-Field view of a *pilT* aggregate subjected to micropipette aspiration but unable to deform and progress as a fluid. Scale bar, 10 μm **(D)** Time-lapse combined view of proliferating WT and *pilT* aggregates inside 10 μm wide PDMS microchannels. Bright-Field: grey; iRFP: red. Time indicated in hs:min. Scale bar, 10 μm. **(E)** Quantification of the surface of aggregates formed by WT (blue) and *pilT* (orange) inside microchannels following proliferation over a 5-hour period. Average values and corresponding standard deviations are indicated with dots and filled regions respectively.